AGU PUBLICATIONS

JGR

Journal of Geophysical Research: Planets

RESEARCH ARTICLE

10.1002/2014JE004645

Global contraction/expansion and polar lithospheric thinning on Titan from patterns of tectonism

Casey Cook-Hallett[1,2], **Jason W. Barnes**[1], **Simon A. Kattenhorn**[3,4], **Terry Hurford**[5], **Jani Radebaugh**[6], **Bryan Stiles**[7], **and Mikael Beuthe**[8]

[1] Department of Physics, University of Idaho, Moscow, Idaho, USA, [2] Natural Sciences Division, North Idaho College, Coeur d'Alene, Idaho, USA, [3] Department of Geological Sciences, University of Idaho, Moscow, Idaho, USA, [4] Now at ConocoPhillips Company, Houston, Texas, USA, [5] NASA Goddard Space Flight Center, Greenbelt, Maryland, USA, [6] Department of Geology, Brigham Young University, Provo, Utah, USA, [7] Jet Propulsion Laboratory,California Institute of Technology, Pasadena, California, USA, [8] Royal Observatory of Belgium, Brussels, Belgium

Key Points:
- Global tectonism is evident as seen through the mapping of its mountains
- A global stress field is responsible for the deformation of Titan's ice shell
- Mountains are a result of either contraction/spin-up or expansion/despinning

Correspondence to:
C. Cook-Hallett,
cook6924@vandals.uidaho.edu

Citation:
Cook-Hallett, C., J. W. Barnes, S. A. Kattenhorn, T. Hurford, J. Radebaugh, B. Stiles, and M. Beuthe (2015), Global contraction/expansion and polar lithospheric thinning on Titan from patterns of tectonism, *J. Geophys. Res. Planets*, *120*, 1220–1236, doi:10.1002/2014JE004645.

Received 12 APR 2014
Accepted 30 MAY 2015
Accepted article online 5 JUN 2015
Published online 30 JUN 2015

Abstract We investigate the underlying physical processes that govern the formation and evolution of Titan's tectonic features. This is done by mapping mountain chains and hills using *Cassini* RADAR data obtained during Titan flybys T3 to T69. Our mapping of mountain chains and hills reveals a global pattern: east-west orientations within 30° of the equator and north-south between 60° latitude and the poles. This result makes Titan one of the few solar system bodies where global processes, rather than regional processes, dominate tectonism. After comparison with five global stress models showing theoretical mountain chain orientations, we suggest that either global contraction coupled with spin-up or global expansion coupled with despinning could explain our observations if coupled with a lithosphere thinner in Titan's polar regions.

1. Introduction

Several moons in our solar system display patterns of tectonism that are driven or modified by global forces [*Collins et al.*, 2009]. Europa's tidally induced fracture patterns [*Geissler et al.*, 1998; *Greenberg et al.*, 1998; *Pappalardo et al.*, 1998b; *Kattenhorn*, 2002], Enceladus's tiger stripes [*Spencer et al.*, 2006; *Porco et al.*, 2006; *Spitale and Porco*, 2007; *Smith-Konter and Pappalardo*, 2008; *Patthoff and Kattenhorn*, 2011], Ganymede's global-expansion-induced normal fault bands [*Golombek*, 1982; *Squyres*, 1982; *Pappalardo et al.*, 1998a; *Bland and Showman*, 2007], and Io's plain ridges [*Bart et al.*, 2004] are examples of global tectonic deformation patterns.

Given its eccentric orbit, proximity to Saturn, and numerous mountain chains, global stresses may affect Titan as well. Images taken with the RADAR Mapper (hereafter, *Cassini* RADAR) aboard the *Cassini* spacecraft have revealed features of high topography referred to as mountains in *Radebaugh et al.* [2007]. While the icy surfaces of Ganymede and Callisto, both of which have comparable size and mass to Titan, are dominated by impact craters, the large-scale coherence of Titan's high topographic features suggests probable formation by global forces [*Radebaugh et al.*, 2007; *Mitri et al.*, 2010].

Synthetic aperture radar (SAR) imagery obtained by *Cassini* RADAR, along with derived topographic information, show evidence for possible contractional or extensional tectonism within Titan's equatorial and polar regions as suggested by *Mitri et al.* [2010], *Radebaugh et al.* [2011], *Solomonidou et al.* [2013], and *Burr et al.* [2013]. At the landscape scale, Titan's fluvial networks include rectangular or trellis morphologies, suggesting formation affected by tectonic structures [*Burr et al.*, 2013]. *Mitri et al.* [2010] propose that isotropic stress from radial contraction, combined with stress from rotational spin-up, would favor the formation of mountain chains in the east-west direction in the equatorial region—like those observed on Titan with both the *Cassini* RADAR [*Radebaugh et al.*, 2007; *Mitri et al.*, 2010] and Visual and Infrared Mapping Spectrometer (VIMS) data [*Barnes et al.*, 2007]. However, Titan's mountains are globally pervasive, implying that a contraction/spin-up model alone is insufficient to explain the global pattern of tectonism.

In our study, we explore the possibility that Titan's tectonism is globally controlled. To do so, we first use *Cassini* RADAR images to map Titan's mountain chains as described in section 2. Section 3 describes how we use the mapping data to look for global patterns in the mountain chain orientations, which we then analyze and

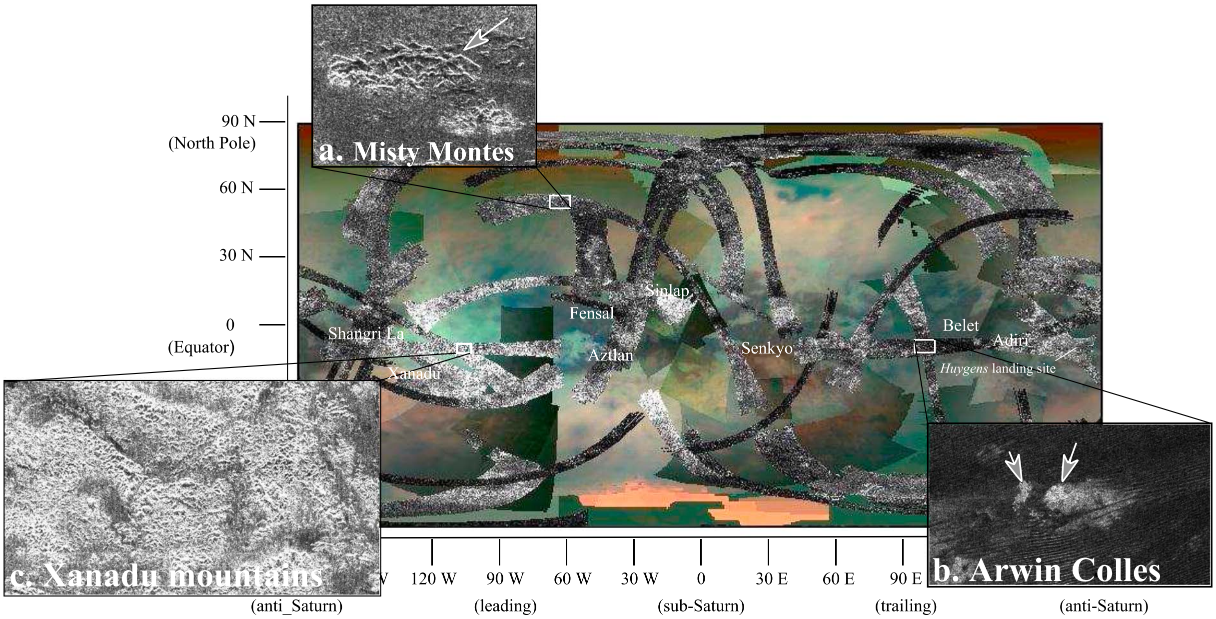

Figure 1. Global cylindrical map of Titan, annotated (names are all IAU accepted), highlighting the two categories of topographic uplifts discussed in this study, as well as a third category, the separately mapped Xanadu region. The map is a combination of low-resolution VIMS images [*Barnes et al.*, 2011] and *Cassini* RADAR swaths from the T3 through T69 flybys. (a) This mountain chain, known as Misty Montes, is located on *Cassini* RADAR swath T23 centered at approximately 57°N, 62°W. (b) This example of Titan hills, named Arwen Colles, is located within the T8 *Cassini* RADAR swath centered at approximately 8°S, 100°E. (c) Centered at approximately 10°S, 103°W, this image is part of the T13 *Cassini* RADAR swath and exemplifies the type of terrain that makes up the Xanadu region.

compare with possible formation mechanisms. Lastly, in section 4, we interpret the geophysical implications of the mountain chains and their orientations in order to create a higher-order picture of the forces affecting Titan's tectonic features and their evolution.

2. Mountain Observations

We construct the maps from a low-resolution cylindrical base map raster [*Barnes et al.*, 2011] layered with higher-resolution *Cassini* VIMS images [*Barnes et al.*, 2009] and *Cassini* RADAR swaths from the T3 through T69 flybys [*Paganelli et al.*, 2007] (Figure 1). We create a global map of the orientations of mountain chains in order to identify the mechanisms driving tectonism on Titan. Therefore, we include surface features that are identified as topographically higher than the surrounding terrain and possess a clear bright-dark pairing within *Cassini* RADAR in our mapping.

2.1. *Cassini* RADAR

Using microwaves instead of visible wavelengths, *Cassini* RADAR actively scans the surface of Titan measuring reflectivity using both passive (radiometry) and active (synthetic aperture, scatterometry, and altimetry) modes (Figure 2). The Ku-band (2.17 cm wavelength) images show surface features that are approximately 1 km and larger [*Janssen et al.*, 2009]. As the spacecraft scans Titan's surface, it receives backscattered energy from each transmitted pulse. By recording the time it takes for the outgoing pulse to be returned to the spacecraft and the wavelength of the returned pulse, *Cassini* RADAR in the SAR mode produces images of highest intensity for a backscattering surface and lower for a forward scattering or absorbing one. The intensity of the backscatter is a combination of the surface reflection (surface roughness and dielectric constant, and orientation relative to the beam) and a subsurface or volume scattering component (dependent on the number density and size of scatterers, the absorptivity of the matrix material, and the dielectric contrast between the matrix and scatterers) [*Barnes et al.*, 2007].

In SAR mode, *Cassini* RADAR looks to the side instead of straight down. This geometry allows it to determine the distance from the spacecraft for each part of the return pulse based on the light travel time delay. The SAR mode process works well for flat surfaces. For mountains, like those shown in Figure 2, as the outgoing radar beam hits the forward slope of a mountain, the beam is reflected back to the spacecraft and is thus recorded as a bright feature. This high-intensity, bright characteristic is a product of radar backscatter for

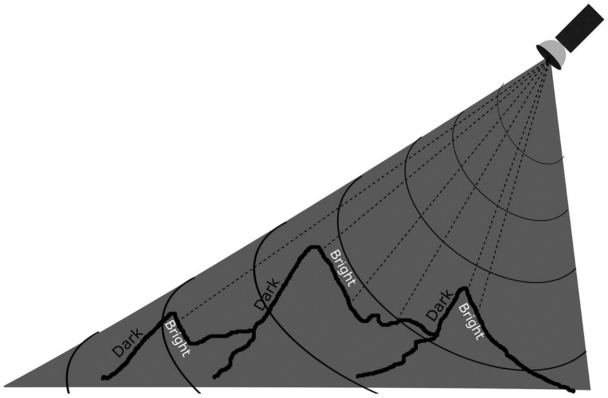

Figure 2. Conceptual cross-section illustration of how *Cassini* RADAR maps Titan's surface. For mountains, like those shown in the figure, as the outgoing radar beam hits the forward slope of a mountain, the time for the beam to return to the spacecraft is recorded and illustrated as a bright feature. The backward slope of the mountain, however, does not record a backscatter and is therefore recorded as a dark feature. This change in intensities is what composes a bright-dark pair and is characteristic of the topographic shading or sharp topographic boundary.

beams reaching the spacecraft at the same time. However, backscatter is not returned (or only returned over an extended period of time) on the back slope of mountains. These features are therefore recorded at a lower intensity, producing a dark feature (Figure 2). This change in intensities is recorded as a bright-dark pair and is characteristic of radar illumination across a sharp topographic boundary [*Elachi et al.*, 2005; *Radebaugh et al.*, 2007]. All mountain chains and hills are therefore identified and mapped using *Cassini* RADAR data in this study, with the bright-dark pairing characteristic considered diagnostic.

2.2. Mountain Chains

Two distinct categories of tectonically formed topographic highs are apparent in *Cassini* RADAR data (Figure 1). The first are those that we define as mountain chains, as exemplified in Figure 1a. Features defined in this category possess a clear bright-dark pairing, a result from SAR illumination of the *Cassini* RADAR-facing slope and shading on the opposite slope. Explicit measurements of heights of individual ranges is not possible with the present data; mountains that do have measured heights are typically 1 km in elevation [*Radebaugh et al.*, 2007]. These mountain chains are generally between 70 and 100 km in length and possess a long, linear nature that is unusual in the solar system and are visually similar to the Appalachian mountains and the Great Basin found on Earth.

To avoid error from exogenously formed mountain-like features, like those that define a crater ring, we only map mountain chains that display a linear nature and are clear of known craters [Sinlap; *Le Mouelic et al.*, 2006, Selk; *Soderblom et al.*, 2010, Paxsi; *Buratti et al.*, 2012, Afekan, and others as discussed in *Neish and Lorenz*, 2012].

2.3. Hills

The second category of topographic highs observed in this study is hills. A hill's descriptor term collis (or plural: colles) is defined by the International Astronomical Union (IAU) as a small hill or knob (Figure 1b). Approximately 18% of Titan's surface is covered by dune fields [*Lopes et al.*, 2010; *Garcia et al.*, 2013]. The hills that are identified in this study are located within the dune fields, primarily in Titan's equatorial latitudes. These features are thought to be of higher surface elevation than the topography that surrounds them based on the redistribution of the surrounding dunes. At this time it is not evident why the hills primarily populate the dune fields. It is possible, however, that the high contrast between the dunes and the hills creates a visual bias and therefore hills are also located at higher latitudes but not visible. High erosion rates and/or dune material may have helped shape the hills.

2.4. Xanadu

The Xanadu region (Figure 1c) contains Titan's most rugged and mountainous terrain [*Radebaugh et al.*, 2011]. We map this region separately to avoid introducing error into global mountain chain orientation measurements due to Xanadu's unique features and possible independent formation as suggested by *Brown et al.* [2011] and *Langhans et al.* [2013].

3. Mapping and Orientations

We map all categories of Titan's topographic highs as polygons in ArcMap. We choose this method because these features encompass a certain coverage area and identification of the bright-dark pairing that characterizes the mountain chains, hills, and Xanadu mountains is dependent on the look direction of *Cassini* RADAR. The radar look direction is an important parameter when analyzing features with a preferred orientation because features may be enhanced or distorted through radar illumination. We mapped Titan's mountains

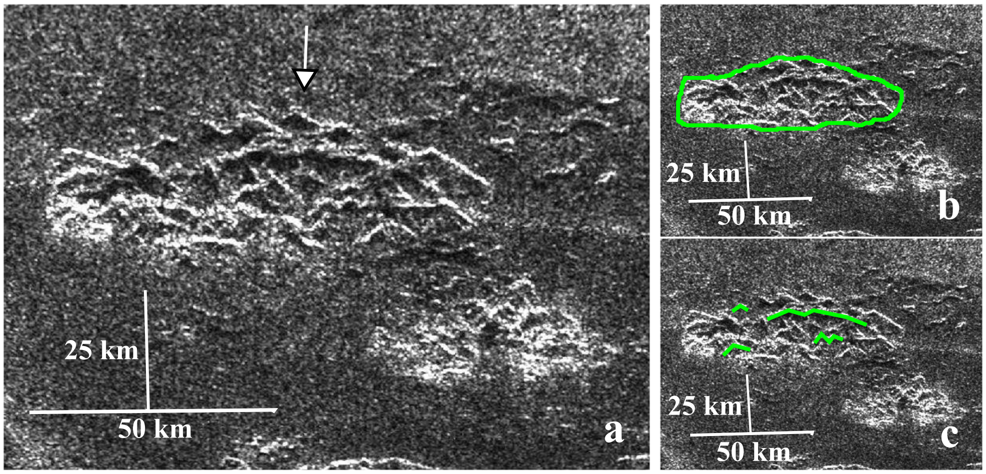

Figure 3. (a) This exemplary mountain chain, known as Misty Montes, located in *Cassini* RADAR swath T23 and centered at approximately 57°N, 62°W, demonstrates the characteristic nature of tectonically formed mountain chains mapped and identified in *Cassini* RADAR by a bright-dark pairing—bright indicating a higher level of backscatter than the dark. The *Cassini* RADAR look direction is indicated by the white arrow. (b) Outlined in green, all mapped mountain chains are marked with a polygon feature class in ArcMap. (c) Green lines highlight the bright-dark pairing which characterizes mountain chains in *Cassini* RADAR.

as polygons to eliminate the look direction bias when establishing orientations. We quantify orientations by using an independent computational algorithm, inputting the length, area, and coordinates of each mapped polygon from ArcMap.

3.1. Mapping

Mountain chains are identified in *Cassini* RADAR by a bright-dark pairing. An exemplary mountain chain, named Misty Montes (Figure 3), is an illustration of the presumed tectonic features in the mountain chain category. The bright green polygon of Figure 3 outlines the lateral boundaries of the mountain chain, providing constraints on the dominant orientation of the mountains.

Outlined in pink, all hills are marked with a polygon feature class in ArcMap. While hills form teardrop shapes within the dunes, only features displaying nonlinear, marbleized variegation of bright-dark pairing are considered to make up a Titan hill. Titan hills are generally 15 to 50 km in length. The hills shown in Figure 4 are known as Arwen Colles.

In order to verify and provide supporting evidence for the validity of our mapped mountain chains and hills, we compare the data to the SARTopo imaging provided by Stiles (for more information on SARTopo, see *Stiles et al.* [2009] and *Lorenz et al.* [2013]), where possible. A shift from bluer to redder colors, as defined by *Stiles et al.* [2009], is indicative of an increase in surface height (Figure 5).

Figure 5 verifies both types of Titan mountain categories. SARTopo imaging shows a color change from a cool blue to a warm yellow and turquoise when passing over the bright-dark pairing defined as the Titan mountain—indicating that the feature is at a higher surface height than the terrain that surrounds it. Similarly, SARTopo imaging shows a variation in color from a cool turquoise to a warm yellow when passing over the feature classified as the Titan hill. Like the mountain chain, the variation in color indicates an increase in surface height. Because surface height on Titan varies among regions, each mapped topographic feature is compared to the surrounding terrain as opposed to a baseline surface elevation for all of Titan.

We focus our mapping of the Xanadu region on unambiguous topographic features displaying clear bright-dark pairings (Figure 6). These features share similar characteristics with those defined in the mountain chain category discussed above and is based on the SARTopo images. Figure 6b demonstrates an increase in surface height over features possessing clear bright-dark pairings, as indicated by the change from a cool blue to a warm yellow. Xanadu mountains are mapped as a polygon feature class in ArcMap with a dark green outline.

Figure 7 shows our global cylindrical map of the mapped mountain chains and hills without the VIMS images or *Cassini* RADAR swaths as background. The pink, bright green, and dark green polygon features denote the

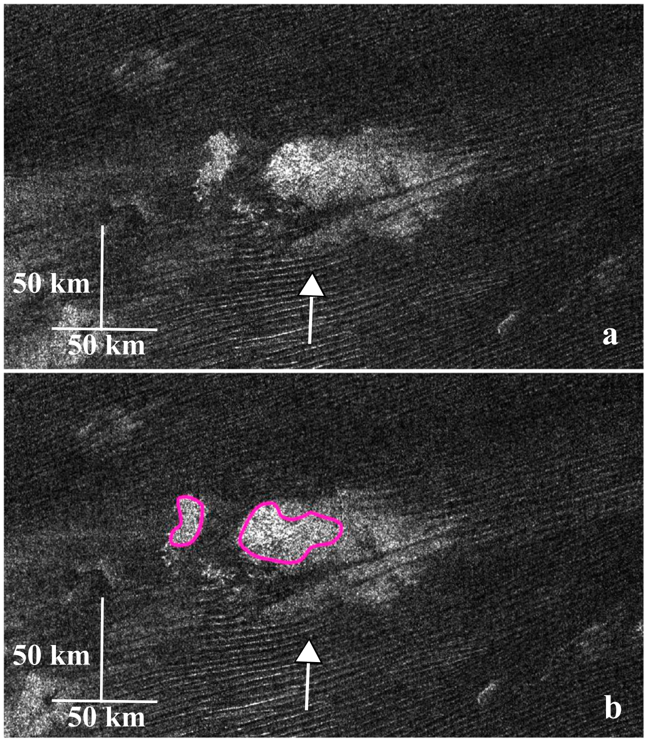

Figure 4. Within the sand dunes in Titan's equatorial latitudes are features described in this paper as hills. These hills are identified by the redistribution of the dune field and a marbling effect of bright-dark pairing and are assumed to be of higher surface elevation than the topography that surrounds them. The *Cassini* RADAR look direction is indicated by the white arrow. (a) This example of Titan hills, known as Arwen Colles, sits within the T8 swath centered at approximately 8°S, 100°E. (b) Outlined in pink, all hills are marked with a polygon feature class in ArcMap. To avoid error in mapping, only features displaying nonlinear bright-dark pairing were considered to make up the Titan hill.

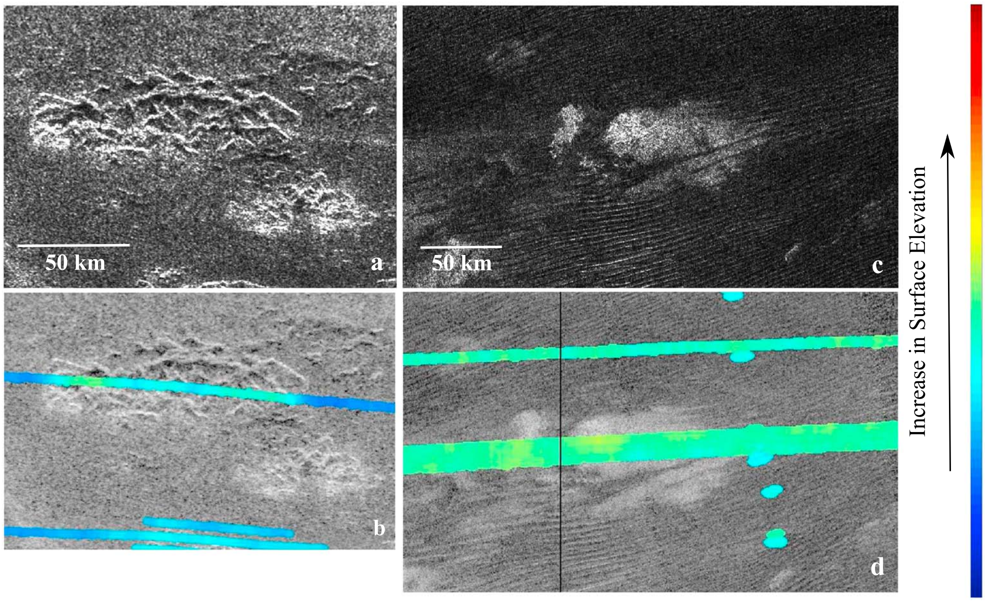

Figure 5. Verification of mountain chains and hills using SARTopo imaging. (a) Misty Montes (Figure 3). (b) The SARTopo image shows a color change over Misty Montes, a cool blue to a warm yellow and turquoise, indicative of an increase in surface height. (c) Arwen Colles (Figure 4). (d) The SARTopo image shows a variation in color from a cool turquoise over the dunes to a warm yellow over the feature classified as hills. This variation is indicative of an increase in surface height, verifying our identification of the area as a hill.

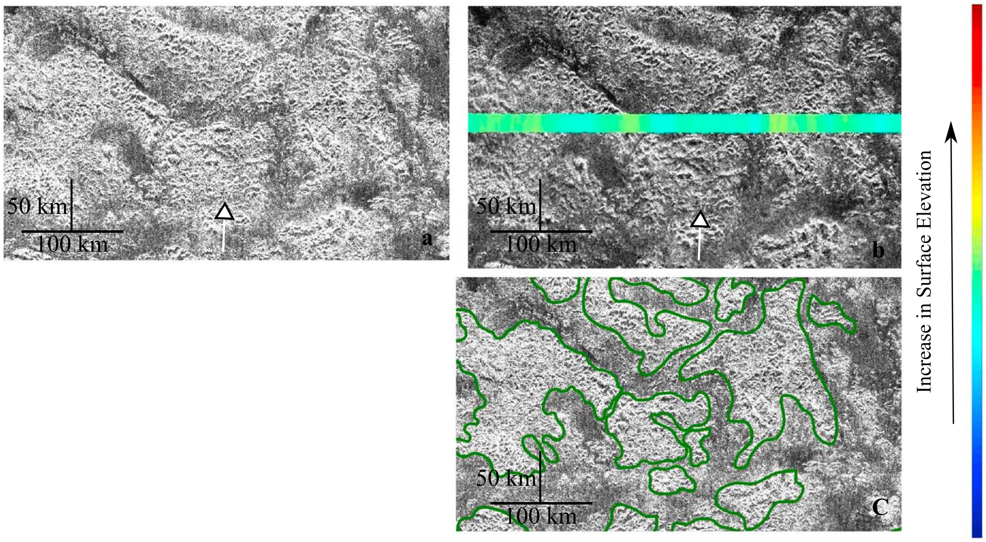

Figure 6. The region defined as Xanadu is composed of Titan's most rugged and mountainous terrain (Figure 1). Xanadu's mountain chains were mapped in a separate category due to their unique characteristics and possible independent formation. The *Cassini* RADAR look direction is indicated by the white arrow. (a) Part of *Cassini* RADAR swath T13 centered approximately at 10°S, 103°W, this image is an example of the terrain which comprises most of the Xanadu region. (b) To avoid error in mapping, SARTopo data are used to determine areas of highest topography and therefore the best areas for mapping mountain ranges. As shown in this image, areas which display bright-dark pairing like that described in the mountain chain category correspond to an increase in surface height. (c) Mountain chains are mapped with a polygon feature class in ArcMap.

mountains interpreted to be tectonic in origin. The purple polygon features are those mountain chains and hills that are confirmed by SARTopo to be topographic highs.

3.2. *Mountainorient*

Our orientation program, deemed *Mountainorient*, calculates the orientation of the line between each vertex within an individual polygon. There is a median of 17 vertices among all the mapped polygons ranging from 5 to 236 vertices within a given polygon. The mathematical slope is determined using the x-y coordinates for each vertex within a given polygon, after a geometric correction for latitude is applied. From the mathematical slope, the angle is determined for each adjacent set of vertices. The orientation of the polygon is then determined by the mode angle of the vertices weighted by length. This orientation angle is then binned to form rose diagrams. The orientation angle for each polygon is measured from 0°N. This process is repeated separately for the mountain chain, hill, and Xanadu data.

Mountainorient then provides a rendering of the global spatial distribution of mountain chain observations by binning polygons within 30° square regions in longitude and latitude and creating a rose diagram. Bins were chosen to be 30° square in order to incorporate enough polygons within a given region to create a statistically significant rose diagram but are small enough that a global pattern may still be interpreted. The two images in Figure 8 are global maps of rose diagrams for the mountain chain category, including an inset of the separately mapped Xanadu region (Figure 8a) and hill category (Figure 8b). The area of each rose diagram is proportional to the area of polygons within each 30° square bin.

3.3. Mapping Results

Quantitative results from *Mountainorient* qualitatively show that both the mountain chains and hills have a higher tendency to be oriented east-west within 30° of the equator, but mountain chains have a higher tendency to be oriented north-south between 60° latitude and the poles. Nonetheless, exceptions to these dominant trends exist in both cases. For example, the 30° square bin lying in the north polar region between 60°W and 90°W qualitatively shows mountain chain orientations trending east-west. Although we generalize both polar regions with north-south orientations, regions such as this may be explained by the presence of Titan's lakes and seas in this region— altering the landscape and therefore causing a mapping bias.

Mountain chains in the northern and southern midlatitudes differ in orientations, however (Figure 8). While no distinct orientations can be assigned, there is a general trend of east-west orientations within the northern

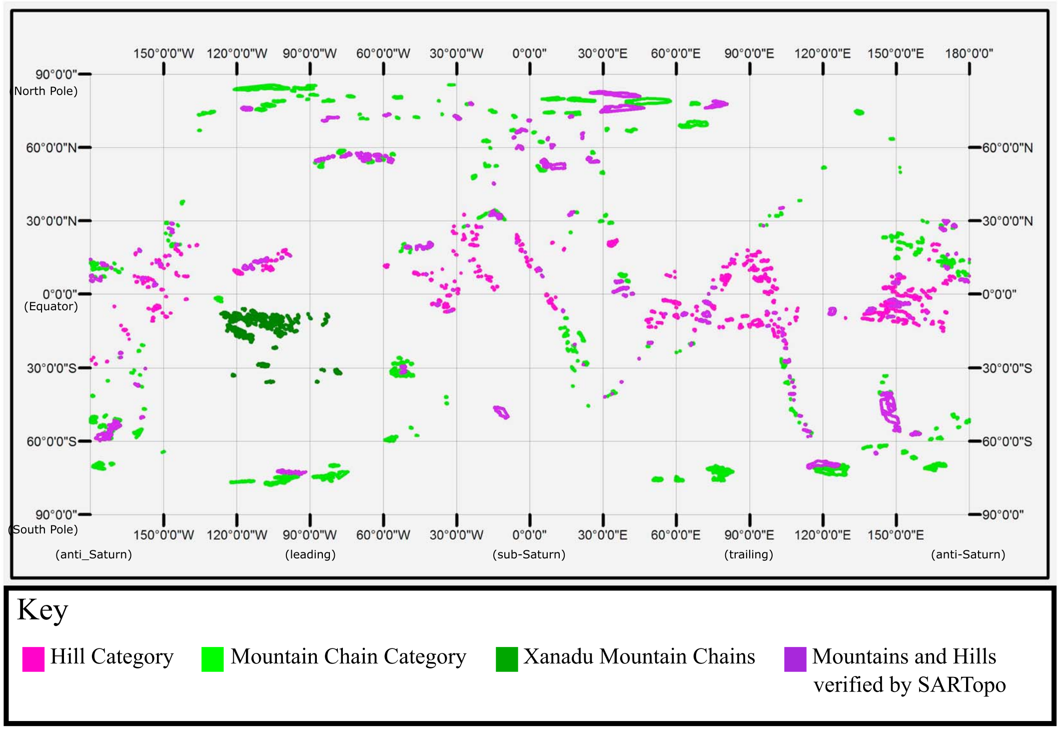

Figure 7. Global cylindrical map (Figure 1) of Titan's mountains without the VIMS images and *Cassini* RADAR swaths as background. The pink, bright green, and dark green polygon features denote mountains identified to be tectonic in origin. Pink are defined as Titan hills, bright green are mountain chains, and dark green are those mountain chains mapped within the Xanadu region. The purple polygon features are those mountain chains and hills that have been identified using SARTopo data to be of a higher surface height than the surrounding terrain.

midlatitudes and variably north-south, east-west, and SW-NE orientations within the southern midlatitudes. Likewise, mountain chains within the Xanadu region display a quantified orientation varying between east-west and SW-NE. This nondistinct orientation may be explained as a result of Xanadu's origin as occupying the site of an ancient impact [*Brown et al.*, 2011] and/or shaped by compressional and extensional tectonism with ongoing erosion from methane rainfall [*Radebaugh et al.*, 2011]. Due to the observational differences between Xanadu and the mountains within the mountain category, the rose diagrams describing the Xanadu mountains are therefore left as an inset to Figure 8a.

It should be noted that the observed mountain chains' orientations show a change from linear within the equatorial and midlatitude regions to more equant at the poles (Figure 9). This morphological change may be as important as the orientation difference.

4. Modeling

Mountain chains can be formed through either compressional or extensional forces, as exemplified on Earth. For example, the Yakima Fold Belt within south central Washington State, USA, is a system of wrinkle ridges that form linear mountain chains. These ridges are anticlines formed through the compression of flood basalt lavas that comprise the upper crust in the region. "Thin-skinned" tectonic features such as these can also describe the fold-thrust belts of the Himalaya and the Appalachians. Contractional structures can also be formed by so-called "thick-skinned" tectonics, in which the faults extend much deeper into the crust. The American Cordillera, which encompass the Rocky Mountains and stretch from southern South America up to Alaska, is an example of such a tectonic feature.

In contrast, linear mountain chains can also form through extension, like those within the Great Basin throughout Western North America. This basin and range region consists of a series of grabens and horsts formed by the stretching of the Earth's lithosphere with uplifted horst blocks creating the linear mountain ranges.

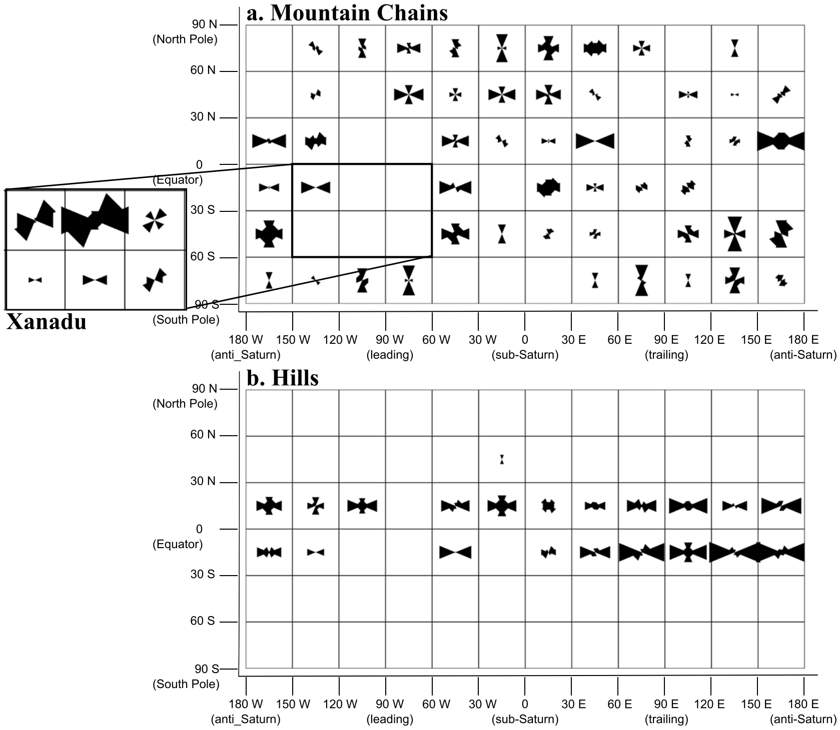

Figure 8. Global maps of rose diagrams for Titan's mountains. (a) Orientations for the mountain chain category, including an inset of those mountains within the Xanadu region, and (b) the hill category orientations. Each rose diagram is a result of binning mapped polygons into 30° square regions. From the global maps of rose diagrams, we note a trend of east-west orientation in Titan's equatorial regions changing to north-south orientation of the mountain chains at the poles.

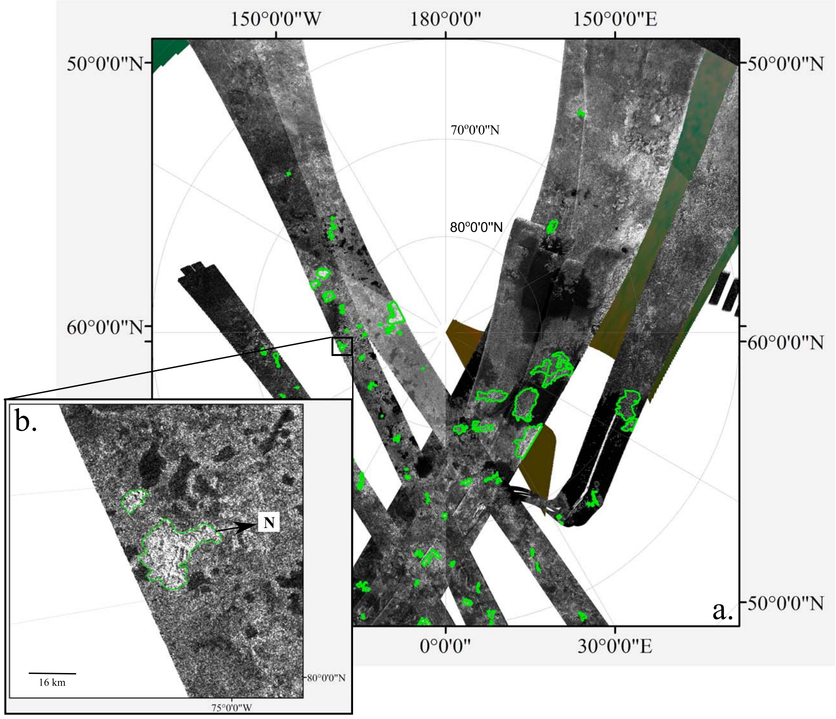

Figure 9. (a) North polar projection of Titan in the region north of 60° latitude with mountain chains shown as green polygons. (b) Located at 82°W, 79°N, the figure highlights examples of the less linear, more equant mountain chains that are prevalent in both the north and south polar regions.

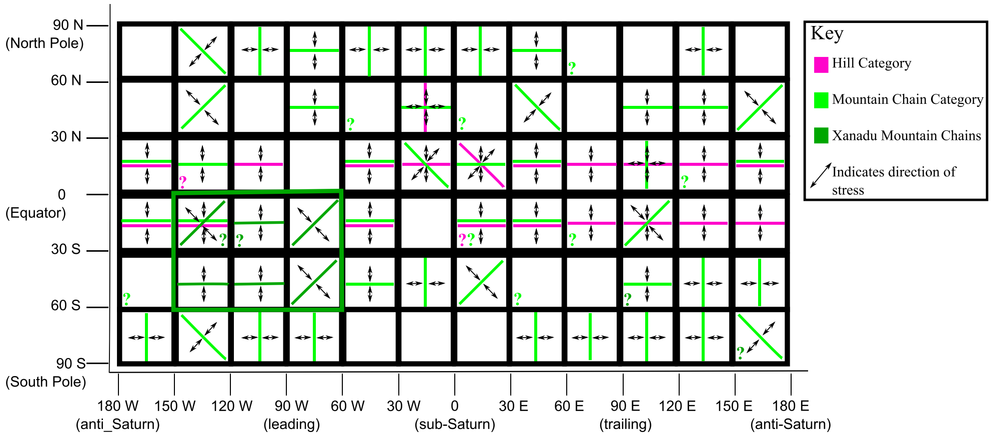

Figure 10. A cartoon of the orientations of the mountain chains and hills within a given 30° square region and the direction of the stress required to form mountains with the given orientation. The given orientations are based on the rose diagrams shown in Figure 8. Like the color scheme of Figure 7, bright green lines indicate the orientations for the mountain chain category, pink for the hill category, and dark green for those mountain chains within the Xanadu region. Question marks, which are also color coded as above, indicate that either no orientation can be concluded from the rose diagram for the given region (marked as a question mark in an otherwise blank square) or an orientation was given however orientation in another direction was also significant. Arrows indicate the direction of stress—can be either compressive or tensile.

The morphological change in mountains on Titan could be a response to regional changes of compression and tension. Current imaging capabilities and high erosion rates do not, however, afford us the ability to investigate Titan's surface with the detail required for fault distinctions. However, by looking at the theoretical stress orientations and magnitudes, we can make reasonable assumptions about the likelihood of mountains being related to faults in the ice shell caused by those stresses.

4.1. Global Stress Models

The existence of mountain chains in distinct orientations that are latitudinally dependent motivates us to test a range of plausible global stress conditions that can generate east-west trending mountains at the equator of a planet and north-south mountains at its poles. Figure 10 illustrates the relationship between the likely principal stresses and mountain orientations.

Gravitational tides, differentiation, orbital migration, and nonsynchronous rotation can be ruled out as possible mechanisms forming the mountain chains and hills, since these do not produce stresses aligned N-S (and hence mountain orientations E-W) along the equator [*Kattenhorn and Hurford*, 2009]. We therefore consider some simple possibilities of stresses produced by changes in rotation rate [*Lorenz et al.*, 2008].

4.1.1. Stress Equations

We construct models showing fault orientations using the following equations [*Melosh*, 2011] which describe the horizontal stress components of the principal stress orientations that develop in a thin, initially unstressed, elastic shell. The horizontal stresses in the north-south (meridional) and east-west (azimuthal) directions are defined as $\sigma_{\theta\theta}$ and $\sigma_{\phi\phi}$, respectively, and are given by

$$\sigma_{\theta\theta} = \frac{1}{3}\Delta f \mu \left(\frac{1+\nu}{5+\nu}\right)(5.0 + 3.0\cos[2\theta]), \tag{1}$$

$$\sigma_{\phi\phi} = \frac{-1}{3}\Delta f \mu \left(\frac{1+\nu}{5+\nu}\right)(1.0 - 9.0\cos[2\theta]), \tag{2}$$

where μ is the rigidity equal to 3.52×10^9 Pa, ν is the Poisson's ratio approximated as to 0.314 [*Mitri et al.*, 2010], and θ is the angular distance from the axis of symmetry.

The variable f is equal to the flatness (oblateness) of the body and Δf the change in flattening from an initially unstressed state. The variable f is calculated using the Darwin-Radau approximation [*Barnes and Fortney*, 2003],

$$\mathbb{C} = \frac{2}{3}\left(1 - \frac{2}{5}\left(\frac{5}{2}\frac{q}{f} - 1\right)^{\frac{1}{2}}\right), \tag{3}$$

where $\mathbb{C}$, the moment of inertia coefficient, is equal to 0.35 [*Barr et al.*, 2010] and q is the centripetal/gravitational acceleration and equal to

$$q = \frac{\omega^2 R^3}{GM}, \tag{4}$$

with R, the mean radius, equal to 2576 km, M the mass of the body equaling 1.3452×10^{23} kg, and G the gravitational constant, 6.67284×10^{-11} $\text{m}^3/(\text{kgs}^2)$. The variable ω is the rotation rate equal to 2π divided by the period.

All model results shown below used the above equations and a compression-positive sign convention.

4.1.2. Global Expansion/Contraction

Any process that changes the shape or volume of a planet can produce tectonic stress [*Head and Solomon*, 1981; *Melosh*, 2011]. The largest-scale change is an alteration in planetary radius caused by heating or cooling [*Melosh*, 2011].

The stresses $\sigma_{\theta\theta}$ and $\sigma_{\phi\phi}$ are equal [*Melosh*, 2011] when considering global expansion/contraction and are therefore equal to

$$\sigma_{\theta\theta} = \sigma_{\phi\phi} = 2\mu\frac{1+\nu}{1-\nu}\frac{\Delta R}{R}, \tag{5}$$

where ΔR is the change in radius and is defined as negative for expansion and positive for contraction.

Stresses that result from global expansion or global contraction are isotropic and produce normal faults under the expansion regime and thrust faults under the contraction regime, extending from the equator to the poles. Both stresses are equal, and therefore faulting (and hence tectonic mountain chains) formed by an expansion/contraction period have no preferred orientations. Therefore, faulting resulting from the change in planetary radius alone is not a fit for the observed global pattern of mountain chains and hills observed on Titan.

4.1.3. Change in Rotation Rate

Stresses as a result of a change in rotation rate are equal to

$$\Delta\sigma_{\theta\theta} = \sigma_{\theta\theta}(\omega_f) - \sigma_{\theta\theta}(\omega_i), \tag{6}$$

$$\Delta\sigma_{\phi\phi} = \sigma_{\phi\phi}(\omega_f) - \sigma_{\phi\phi}(\omega_i), \tag{7}$$

where $\sigma_{\theta\theta}(\omega_{f/i})$ and $\sigma_{\phi\phi}(\omega_{f/i})$ are calculated using equations (1) and (2) with the initial and final rotation rates, ω_i and ω_f.

We determine fault orientation using Anderson's theory of faulting [*Anderson*, 1951]. Assigning each of the three principal stresses, σ_1, σ_2, and σ_3, to either the north-south stress, the east-west stress, or the vertical stress based on relative magnitudes, we are able to determine whether normal, thrust, or strike-slip faulting occurs at the surface. The vertical stress is related to the weight and density of the overlying ice by [*Fossen*, 2010]

$$\sigma_v = \rho g z, \tag{8}$$

where z is the distance into the ice shell. For Titan, using the density of ice *I* (equal to 0.934 g/cm^3) and a shell thickness of 100 km [*Nimmo and Bills*, 2010], the vertical stress is calculated to be 0.0124 bar/km. Note that the vertical stress is equal to 0 at the surface. By definition of the compression-positive convention, σ_1 is vertical in a normal fault regime, σ_2 is vertical in a strike-slip fault regime, and σ_3 is vertical in a thrust fault regime [*Fossen*, 2010]. Also, $\sigma_1 > \sigma_2 > \sigma_3$, where σ_1 is most compressive.

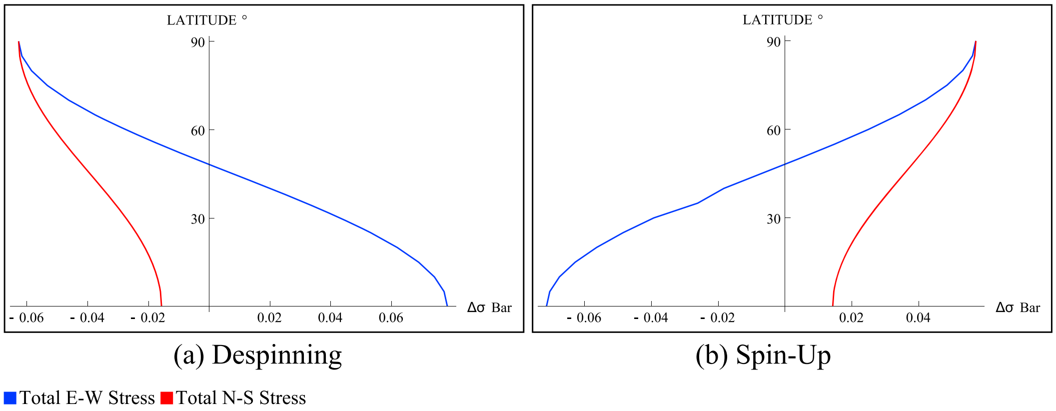

(a) Despinning (b) Spin-Up

Figure 11. Stress changes due to a change in spin rate, $\Delta\sigma$ versus latitude. As Titan's spin rate changes, strike-slip faults (orientated in a NE-SW and NW-SE conjugate pattern) result in the equatorial region. (a) As the spin rate decreases, normal faulting results in the polar regions (north of 48° latitude). The fault orientations (and hence mountain orientations) are in the east-west direction as a result of the more tensile north-south stress, $\sigma_{\theta\theta}$. (b) Similarly, east-west faulting (and hence mountain orientations) result from an increase in Titan's rotation rate. However, the fault type changes from normal to thrust due to the designation of the vertical stress as σ_3.

Considering initial periods ± half a Titan day, the stress field as a result of a change in rotation rate (spin-up or despinning) is anisotropic within both the equatorial region (extending from +48° to −48°) and the polar regions (extending from ±48° to 90°) (Figure 11).

As Titan's spin rate changes, strike-slip faults (orientated in a NE-SW and NW-SE conjugate pattern) result in the equatorial region because the principal stress, σ_2, is assigned as the vertical stress. In the polar regions, as the spin rate decreases, normal faulting results from a designation of σ_1 as the vertical stress. The fault orientations (and hence mountain chain orientations) are in the east-west direction as a result of the more tensile north-south stress, $\sigma_{\theta\theta}$. Similarly, east-west faulting (and hence mountain chain orientations) result from a increase in Titan's rotation rate. However, the fault type changes from normal to thrust due to the designation of the vertical stress as σ_3. This is the same result reported by *Melosh* [1977]. The faulting, however, does not match the pattern of mountain chains and hills observed on Titan in either the equatorial or polar regions.

4.1.4. Expansion/Contraction With Change in Rotation Rate

Next, we model Titan's stress field resulting from global contraction with spin-up and global expansion with despinning, a combination of the two previous models (Figure 12). All changes in planetary radius alter the rate of rotation due to the conservation of angular momentum. In such cases, the resulting horizontal field is everywhere anisotropic.

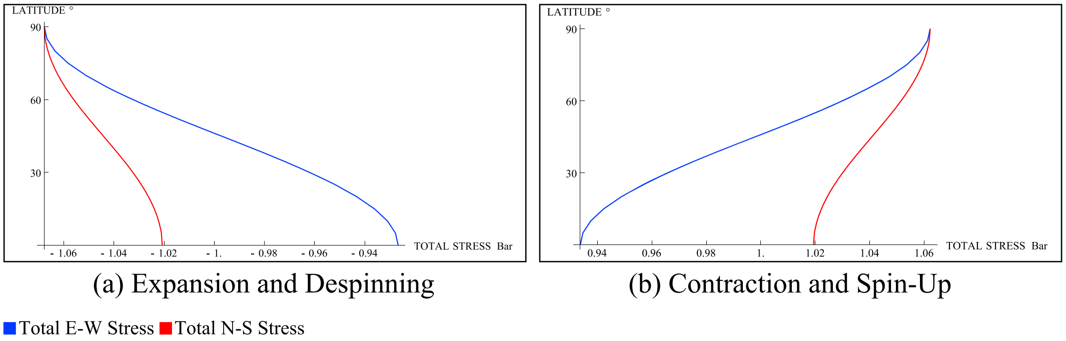

(a) Expansion and Despinning (b) Contraction and Spin-Up

Figure 12. Total stress, expansion with despinning and contraction with spin-up versus latitude. In the expansion with despinning case, the vertical stress is always the maximum principal stress, σ_1, whereas the north-south stress, $\sigma_{\theta\theta}$, is the minimum stress, σ_3. Therefore, east-west normal faulting (and hence mountain chain orientation) occurs everywhere. In contrast, in the contraction with spin-up case, the vertical stress is always the minimum principal stress, σ_3, and the north-south stress, $\sigma_{\theta\theta}$, the most compressive stress, σ_1. Therefore, east-west thrust faulting (and hence mountain chain orientation) occurs everywhere.

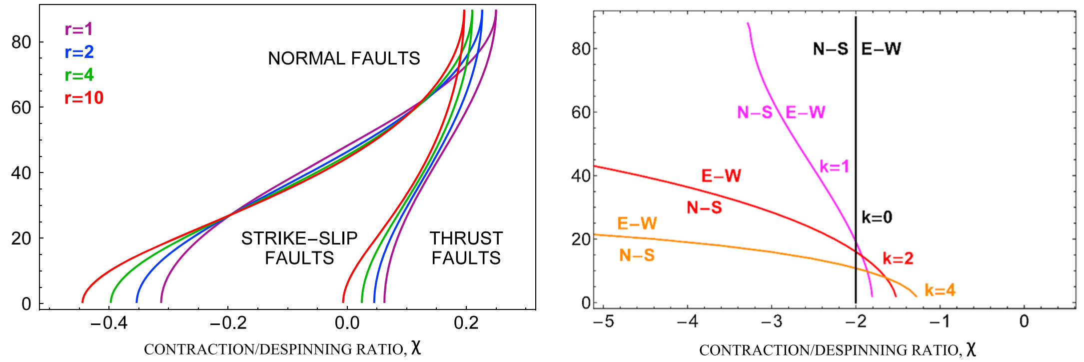
(a) FAULT STYLE

(c) ENLARGEMENT OF THIN ZONE (r=2)

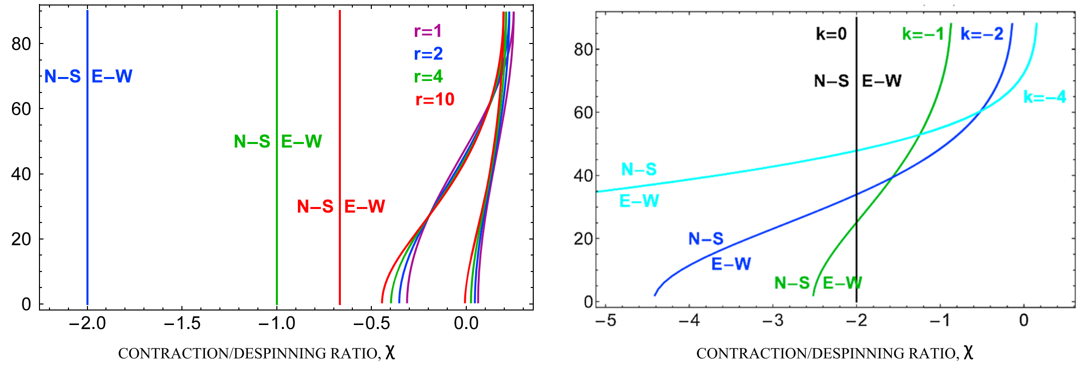
(b) ORIENTATION OF NORMAL FAULTS

(d) REDUCTION OF THIN ZONE (r=2)

Figure 13. Faulting and orientation for simultaneous expansion and despinning for a generic Titan with a Poisson ratio equal to 0.33. (a) Boundaries of the areas with a given fault style for a range of ice shell thickness ratios. (b) The threshold beyond which the orientation of the normal faults change from north-south to east-west. The threshold for $r = 1$ is at infinity because the normal faults never switch orientation when the elastic thickness is constant. The boundaries of the areas with a given fault style are shown as in Figure 13a. (c and d) Enlargement of the thin zone with $r = 2$. The value k refers to the size of the thin zone. For polar lithospheric thinning, negative values correspond to a reduction and positive values to expansion. A k value equal to 0 is the same as the curve mapping $r = 2$ and therefore indicates no expansion or reduction of the thin zone.

For the expansion with despinning case, the vertical stress is always the principal stress σ_1 and the north-south stress, $\sigma_{\theta\theta}$, the most tensile stress, assigned as σ_3. Therefore, east-west normal faulting (and hence mountain chain orientation) occurs everywhere except at the poles.

For the contraction with spin-up case, the vertical stress is always the principal stress, σ_3, and the north-south stress, $\sigma_{\theta\theta}$, the most compressive stress, assigned as σ_1. Therefore, east-west thrust faulting (and hence mountain chain orientation) occurs everywhere.

We therefore conclude that these contraction/spin-up and expansion/despinning models do not by themselves explain our observations of Titan's global patterns. It is not apparent that a single model, nor a combination of a change of rotation rate and expansion/contraction, can provide the sources of compression and/or tension needed to form the observed mountain chain orientations, specifically those mountain chains with north-south orientation at the poles.

4.1.5. Expansion/Contraction With Change in Rotation Rate and Variation in Shell Thickness

We therefore consider the possibility of nonuniform lithospheric thickness, as explored by *Beuthe* [2010], with lithosphere defined as the outer portion of a body that responds either elastically or fractures as a brittle solid when stress is applied [*Barrell*, 1914]. *Beuthe* [2010] describes the generation of north-south oriented tectonic features in the polar regions of planets through the generation of contraction and spin-up or expansion and despinning with a lithosphere thinner at the poles.

Using the thin shell elastic model, Figure 13 is constructed for a generic Titan using a Poisson ratio, ν, of 0.33 and the equator-to-pole thickness ratio of r:

$$r = \frac{h_E}{h_P}, \tag{9}$$

with h_E the equatorial lithosphere thickness and h_P the polar lithosphere thickness.

The proportion between contraction/expansion and spin rate is parameterized by the contraction/despinning ratio χ:

$$\chi = -\frac{\bar{w}_0}{\bar{w}_2}, \tag{10}$$

which is 0 if there is only a change in spin rate and negative when considering either expansion with despinning or contraction with spin-up. The parameters $\bar{w}_0$ and $\bar{w}_2$ describe degree 0 and degree 2 in the expansion of the nondimensional transverse displacement—the inward and outward motion of the elastic ice shell caused by contraction/expansion and spin-up/despinning—with $\bar{w}_0$ describing contraction and $\bar{w}_2$ describing oblateness. Figure 13 considers the case of contraction/expansion with despinning when combined with a thin polar lithosphere. Note that when considering contraction/expansion with spin-up, the stress values change sign. Therefore, the resulting model for χ versus latitude is the same curve but with different faulting styles (i.e., normal faulting in Figure 13 changes to thrust faulting and thrust faulting on Figure 13 changes to normal faulting).

Figure 13a shows the faulting style of a Titan with simultaneous expansion and despinning. For given χ, the curves indicate the boundaries between the tectonic provinces. Each set of curves is formed by modeling the latitude versus χ using the following equations derived using equations provided in *Beuthe* [2010]:

$$\cos[2\theta] = \frac{1}{9}\left(1 + \frac{4\chi(5+\nu)}{1-\nu}\right), \tag{11}$$

$$\cos[2\theta] = \frac{1}{3}\left(-5 + \frac{4\chi(5+\nu)}{1-\nu}\right), \tag{12}$$

where θ is the colatitude.

As stated above, a negative χ corresponds to an expansion with despinning event. Using this type of event as an example, as χ decreases due to an increase of $\bar{w}_0$ (i.e., becoming more expansion dominated), the faulting style changes from strike-slip in the equatorial region and normal in the polar region to normal faulting throughout the surface. This is expected and shown in Figure 12. Note that as r, the equator-to-pole thickness ratio, increases, the expansion rate must increase in order for fault type to change with latitude.

Titan, however, has a change in fault orientation with respect to latitude. Figure 13b shows the threshold beyond which the orientation of the normal faults change from north-south to east-west in the case of expansion with despinning. The threshold for $r = 1$ is at infinity because the normal faults never switch orientation when the elastic thickness is constant. As r increases, however, a latitudinal change in the orientation of faulting does not occur simply by stating that the lithospheric thickness is thinner in the polar regions. Any change in normal or thrust fault orientation occurs over all latitudes simultaneously and therefore cannot account for the mountain orientations on Titan.

By changing the size of the thin zone, however, such a change in orientation can be achieved (Figures 13c and 13d). Models c and d of Figure 13 are shown with an equatorial to polar thickness ratio $r = 2$ or, in other words, a lithosphere that is 2 times thicker at the equator than at the poles. The value k refers to the size of the thin zone defined within the interval $[0,\pi/2]$ that is nonlinearly altered by a function Ψ_k [*Beuthe*, 2010] equal to

$$\Psi_k = \frac{\pi}{2}\frac{\sinh\left(\frac{2k\theta}{\pi}\right)}{\sinh(k)}, \quad \text{if} \quad k>0 \quad \text{or} \quad \Psi_k = \frac{\pi}{2}\frac{\sinh\left(\frac{2k\theta}{\pi}\right)}{\tanh(k)}, \quad \text{if} \quad k<0. \tag{13}$$

For polar lithospheric thinning, negative values correspond to a reduction and positive values to expansion. For example, in the case of a reduction of the thin zone, the area defined by the value h_P, the polar lithospheric thickness, decreases in size poleward as the value of k becomes more negative. Note that a k value equal to 0 is the same as the curve mapping $r = 2$ and therefore indicates no enlargement or reduction of the thin zone [*Beuthe*, 2010].

Figures 13c and 13d are interpreted as follows: For $k = 0$ and $\chi = -2$, the resulting fault pattern has no preferred orientation, since both the N-S and E-W stresses are equal. For $k = 2$, corresponding to an enlargement of the thin zone (Figure 13c), fault orientation changes latitudinally at the point when the curve intersects a vertical line passing through $\chi = -2$. Therefore, N-S faulting (and hence mountain chains) occurs equatorward of approximately 15° latitude and E-W faulting (and hence mountain chains) occurs poleward of approximately 15° latitude. This pattern is the same for all positive k values, with the exception of the latitudinal position at which they switch orientation. In Figure 13c, where the thin zone is getting bigger, this "switch position" decreases in latitude as the value of k increases.

For the case of a reduction of the thin zone, N-S faulting (and hence mountain chains) can form in the polar regions (Figure 13d). Consider a k value of -2. The switch to E-W orientated faults (and hence mountain chains) to N-S orientated faults (and hence mountain chains) occurs at approximately 35°. As before, this switch position increases in latitude as the value of k increases.

It is important to note that if the size of the thin zone varies ($k \neq 0$), a change in fault orientations that is latitude dependent can result, as needed to account for observed mountain chain orientations. Nonetheless, it is also required that the value of $\chi < -0.7$ for the range of $r = 1, 2, 4, 10$. Also, for smaller variability in ice shell thickness from the equator to the poles ($r < 4$), the latitudinal dependent fault change occurs at $\chi < -1$, indicating that the expansion or contraction term dominates over changes in spin rate in controlling latitudinal changes in fault orientation.

Therefore, we have found a theoretical model that matches the observed pattern of mountain chains and hills on Titan—east-west faulting in the equatorial region along with north-south faulting in the polar regions can be explained through the model of global contraction and spin-up or global expansion and despinning combined with a lithosphere thinner in the polar regions that has a thin zone that is reducing in size (i.e., an area of thinning that is decreasing in size poleward).

5. Discussion

While tectonic features can often be formed by local or regional processes, on some icy moons they form a global pattern. The pattern is generally the result of global deformation of the body's ice shell, generating a global stress field that may result in a faulting pattern at the surface [*Vening-Meinesz*, 1947]. Mapping of Titan's mountain chains and hills reveals a global pattern of faulting indicating a global stress field.

5.1. Results

We can now place Titan into the small category of solar system bodies with global stress patterns due to the mountain and hill orientations displaying a general pattern of east-west orientation within 30° of the equator, north-south within 30° of the poles, and a mix of both in the 30°–60° latitude range. While we cannot conclude whether Titan's mountains were, or continue to be, formed by contraction or expansion, there is evidence for both throughout the solar system. For instance, the surfaces of Mars [*Sleep*, 1994; *Anguita et al.*, 2006; *Nahm and Schultz*, 2010], Mercury [*Watters et al.*, 2009; *Beuthe*, 2010; *Byrne et al.*, 2014], and Io show compressional tectonic features, whereas many icy satellites, such as Ganymede, Enceladus, Europa, and the Moon [*Watters et al.*, 2012; *Banks et al.*, 2012], show evidence of extension and normal faulting.

On Titan, if mountain chain and hill orientations result from thrust faults (resulting from global contraction), then an east-west pattern in the equatorial region is possible if coupled with the spin-up stress field (Figure 12). However, this pattern would also extend into the polar regions. A change in rotation rate can also produce fields of east-west thrust or normal faulting; however, this occurs in the polar regions with strike-slip faulting in the equatorial region. Therefore, neither model can account for the north-south thrust or normal faulting at the poles (Figure 14).

It is the unaccounted for north-south orientations in polar regions that lead us to conclude that the global stress models in Figures 11 and 12 do not provide a good fit for explaining the orientations of Titan's mountain chains and hills. This is why we consider a change in the mean planetary radius (contraction or expansion) coupled with planetary flattening due to a change in the rotational period (spin-up or despinning) which can theoretically result in north-south faulting in the polar regions and east-west faulting at the equator, as long as the body's lithosphere has a thin zone that is reducing in the polar regions [*Beuthe*, 2010] (Figure 14). Variation of lithospheric thickness on Titan may have resulted from a tidally heated, conductive ice shell, as evidenced by topographic mapping [*Nimmo and Bills*, 2010; *Lorenz et al.*, 2013].

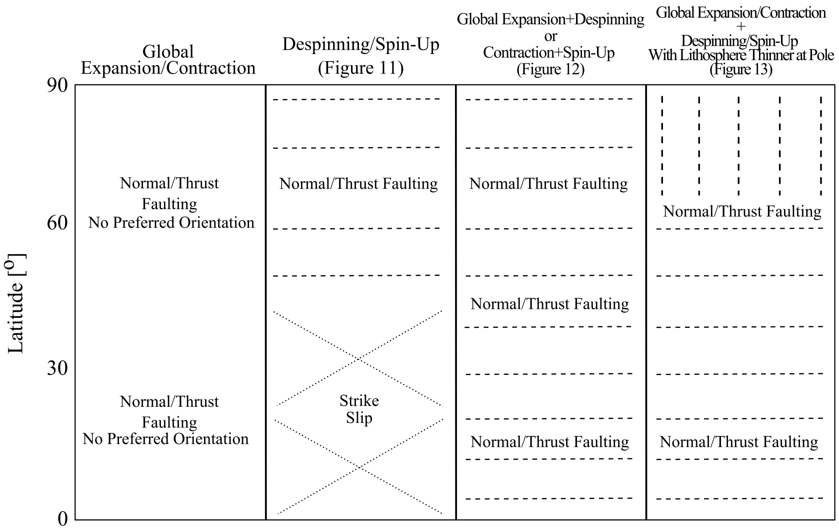

Figure 14. Faulting patterns as a result of the various forms of stress illustrated in Figures 11–13. We find a match to the observed mountain chain and hill orientations when considering contraction and spin-up or expansion and despinning combined with a lithosphere thinner in the polar regions than at the equator. The southern hemisphere reflects that of the northern hemisphere shown in this figure.

5.2. Implications and Caveats

Although we suggest that Titan's mountain chains and hills may have been formed through either a combination of global contraction with spin-up or global expansion with despinning and a lithosphere thinner in the polar regions, we recognize that either mechanism may be difficult to achieve.

The spinning-up of Titan can be caused by the body's response to Saturn's gravitational pull during its orbital migration at pericenter. However, it is not certain whether the amount of spin-up at pericenter would provide the appropriate amount of stress needed for the thrust faulting to occur. On the other hand, spin-up can be the response to planetary contraction due to the moderate cooling of Titan's low ammonia concentrated ocean, which is what would be expected within the most recent 100 million years (S. Vance, personal communication, 2014).

Similarly, a despinning event on Titan could result from the body's response to Titan's orbital migration outward. As in the case of spin-up, despinning can also be the response to the change of the planetary radius. In this case, however, despinning is the response to the expansion due to the freezing of Titan's ice I shell. On the other hand, global expansion could result from Titan's despinning early in its history. This is where models for the despinning and expansion of Titan suffer. A high despinning rate, more than what is expected during Titan's outward orbital migration, would be needed for the formation of normal faults [*Pechmann and Melosh*, 1979]. This rate may have been present early in Titan's history; however, the time it would take for Titan to produce mountain chains and hills is much longer than the relatively short amount of time that it presumably took for Titan to reach its current rotational period.

The above discussion is not to say that global contraction with spin-up nor that global expansion with despinning answers the question in entirety of how Titan's mountain chains and hills were (or are currently) formed. The low stress magnitudes calculated—magnitudes no greater than 1.06 bar or 106 kPa—and used to form the models are much lower than would be expected for fault formation. This is because the creation of faults is dependent on satisfaction of the Coulomb failure criterion, which states that the critical necessary ratio of shear and normal stress is needed to cause shear failure. Low stress magnitudes will be overcome by a dominant overburden stress at shallow depths, and therefore, no faulting will occur.

Still, the low stress magnitudes provide a context for understanding principal stress directions and hence fault orientations and could be swaying the perception of what is occurring within Titan's ice shell. For example, liquid hydrocarbons within Titan's ice shell require a much lower stress rate for fault formation and therefore suggests that faults could be more likely in the event that such liquids introduce a fluid pressure that reduces the differential stress needed for frictional failure [*Liu et al.*, 2013].

Calculations of strain would provide further insight for the parameters required for fault formation on Titan. However, strain calculations require observable information such as mountain chain and hill height relative to background reference elevation and faulting type. These calculations, which would then be compared to theoretical strain calculations, cannot currently be done for Titan. A small sample of mountain chain heights has been measured and cannot be generalized for all of Titan. Furthermore, only minimum strain calculations could be made given Titan's high erosion rates.

Also, the models presented in Figure 13 suggest that the ratio of change in planetary radius to spin rate, χ, as well as the amount at which the size of the polar thin zone is reducing or expanding, k, influences the orientation of fault (and hence mountain chain) formation. If either or both parameters have changed within the history of Titan, this may explain the exceptions of mountain chain orientations that occur within both the equatorial and polar regions, as well as the overlap in orientations of mountain chains within the northern and southern midlatitudes.

Determination of whether Titan is (or has experienced in the past) globally contracting or expanding requires more work. The identification of fault type (thrust faults if contraction, normal faults if expansion) would provide the most useful indication; however, Titan's thick atmosphere and high erosion rate on its surface makes fault identification difficult [*Lopes et al.*, 2010].

6. Conclusion

Titan's mountain chains and hills form a global pattern: They are preferentially orientated east-west at the equator and north-south at the poles, with overlap in the midlatitudes. Global stress models that show either tidal response changes or spin rate changes alone cannot account for the faulting pattern (whether thrust or normal) that would be needed to form the observed mountain chains and hills on Titan. We therefore conclude that this pattern may be a result of Titan's ice shell being thinner at the poles while globally contracting and spinning-up or expanding and despinning.

We suggest further observations, such as higher-resolution and/or stereo imagery, of the mountain chains and hills in order to conclusively determine Titan's global stress field during the period of tectonic mountain formation. Better imaging of the mountain chains and hills, perhaps with the use of an airplane mission to Titan [*Barnes et al.*, 2012], could help to identify faulting and accurately constrain the stresses responsible for the faulting/tectonics and, hence, provide us with the mechanisms driving mountain formation on Titan.

Acknowledgments
Thanks to Alex Patthoff and Emily Martin for discussions and lessons on ArcGIS. The authors acknowledge support from NASA Outer Planets Research Program grant NNX10AQ10G. M. Beuthe is supported by the PRODEX program managed by the European Space Agency and the Belgian Federal Science Policy Office. The portion of this research carried out by B. Stiles was done so at the Jet Propulsion Laboratory, California Institute of Technology, under contract with the National Aeronautics and Space Administration. The data to support this article are from the National Aeronautics and Space Administration (NASA). ArcGIS shapefiles are available at the following website:r5d4.barnesos.net/GlobalPatternsofTectonism.

References

Anderson, E. M. (1951), *The Dynamics of Faulting and Dyke Formation With Applications to Britain*, Oliver and Boyd, Edinburgh, Scot.

Anguita, F., C. Fernandez, G. Cordero, S. Carrasquilla, J. Anguita, A. Nunez, S. Rodriguez, and J. Garcia (2006), Evidences for a Noachian-Hesperian orogeny in Mars, *Icarus*, *185*, 331–357.

Banks, M. E., T. R. Watters, M. S. Robinson, L. L. Tornabene, L. Ojha, and N. R. Williams (2012), Morphometric analysis of samll-scale lobate scarps on the Moon using data from the Lunar Reconnaissance Orbiter, *J. Geophys. Res.*, *117*, E00H11, doi:10.1029/2011JE003907.

Barrell, J. (1914), The strength of the Earth's crust, *J. Geol.*, *22*, 289–314.

Barnes, J. W., and J. J. Fortney (2003), Measuring the oblateness and rotation of transiting extrasolar giant planets, *Astrophys. J.*, *588*, 545–556.

Barnes, J. W., et al. (2007), Near-infrared spectral mapping of Titan's mountains and channels, *J. Geophys. Res.*, *112*, E11006, doi:10.1029/2007JE002932.

Barnes, J. W., et al. (2009), VIMS spectral mapping observations of Titan during the Cassini prime mission, *Planet. Space Sci.*, *57*, 1950–1962.

Barnes, J. W., et al. (2011), Organic sedimentary deposits in Titan's dry lakebeds: Probable evaporite, *Icarus*, *216*, 136–140.

Barnes, J. W., et al. (2012), AVIATR—Aerial Vehicle for In-situ and Airborne Titan Reconnaissance, *Exp. Aston.*, *33*, 55–127.

Barr, A. C., R. I. Citron, and R. M. Canup (2010), Origin of a partially differentiated Titan, *Icarus*, *209*, 858–862.

Bart, G. D., E. P. Turtle, W. L. Jaeger, L. P. Keszthelyi, and R. Greenberg (2004), Ridges and tidal stress on Io, *Icarus*, *169*, 111–126.

Beuthe, M. (2010), East-west faults due to planetary contraction, *Icarus*, *209*, 795–817.

Bland, M. T., and A. P. Showman (2007), The formation of Ganymede's grooved terrain: Numerical modeling extensional necking instabilities, *Icarus*, *189*, 439–456.

Brown, R. H., J. W. Barnes, and H. J. Melosh (2011), On Titan's Xanadu region, *Icarus*, *214*, 556–560.

Buratti, B. J., C. Sotin, K. Lawrence, R. H. Brown, S. Le Mouelic, J. M. Soderblom, J. Barnes, R. N. Clark, K. H. Baines, and P. D. Nicholson (2012), A newly discovered impact crater in Titan's Senkyo: Cassini VIMS observations and comparison with other impact features, *Planet. Space Sci.*, *60*, 18–25.

Burr, D. M., S. A. Drummond, R. Cartwright, B. A. Black, and J. T. Perron (2013), Morphology of fluvial networks in Titan: Evidence for structural control, *Icarus*, *226*, 742–759.

Byrne, P. K., C. Klimczak, A. M. Celal Sengor, S. C. Solomon, T. R. Watters, and S. A. Hauck (2014), Mercury's global contraction much greater than earlier estimates, *Nat. Geosci.*, *7*, 301–307.

Collins, G. C., W. B. McKinnon, J. M. Moore, F. Nimmo, R. T. Pappalardo, L. M. Prockter, and P. M. Schenk (2009), Tectonics of the outer planet satellites, in *Planetary Tectonics*, pp. 264–350, Cambridge Univ. Press, Cambridge, U. K.

Elachi, C., et al. (2005), Cassini RADAR views the surface of Titan, *Science*, *308*, 970–974.

Fossen, H. (2010), *Structural Geology*, Cambridge Univ. Press, New York.

Garcia, A., et al. (2013), Global mapping and characterization of Titan's dune fields with Cassini: Correlation between RADAR and VIMS observations, 44th Lunar and Planetary Science Conference, Houston, Tex., 2013 March.

Geissler, P. E., et al. (1998), Evolution of lineaments on Europa: Clues from Galileo multispectral imaging observations, *Icarus*, *135*, 107–126.

Greenberg, R., P. Geissler, G. Hoppa, B. R. Tufts, D. D. Durda, R. Pappalardo, J. W. Head, R. Greeley, R. Sullivan, and M. H. Carr (1998), Tectonic processes on Europa: Tidal stresses, mechanical response, and visible features, *Icarus*, *135*, 64–78.

Golombek, M. P. (1982), Constraints on the expansion of Ganymede and the thickness of the lithosphere, *J. Geophys. Res.*, *87A*, 77–83.

Head, J. W., and S. C. Solomon (1981), Tectonic evolution of the terrestrial planets, *Am. Assoc. Adv. Sci.*, *4503*, 62–76.

Kattenhorn, S. A. (2002), Nonsynchronous rotation evidence and fracture history in the Bright Plains region, Europa, *Icarus*, *157*, 582–602.

Kattenhorn, S. A., and T. Hurford (2009), Tectonics of Europa, in *Europa*, edited by R. T. Pappalardo, W. B. McKinnon, and K. Khurana, pp. 199–236, Univ. of Arizona Press, Tucson, Ariz.

Langhans, M., J. I. Lunine, and G. Mitri (2013), Titan's Xanadu region: Geomorphology and formation scenario, *Icarus*, *223*, 796–803.

Janssen, M. A., et al. (2009), Titan's surface at 2.2-cm wavelength imaged by the Cassini RADAR radiometer: Calibration and first results, *Icarus*, *200*, 222—239.

Le Mouelic, S., et al. (2006), Mapping and interpretation of Sinlap crater on Titan using Cassini VIMS and RADAR data, *J. Geophys. Res.*, *113*, E04003, doi:10.1029/2007JE002965.

Liu, Z., J. Radebaugh, R. A. Harris, and E. H. Christiansen (2013), Role of fluids in mechanics of overthrust faulting on Titan, Abstract P52B-02 paper presented at 2013 Fall Meeting, AGU, San Francisco, Calif., 2013 Dec.

Lopes, R. M. C., et al. (2010), Distribution and interplay of geologic processes on Titan from Cassini RADAR data, *Icarus*, *205*, 540–558.

Lorenz, R. D., B. W. Stiles, R. L. Kirk, M. D. Allison, P. Persi del Marmo, L. Less, J. I. Lunine, S. J. Ostro, and S. Hensley (2008), Titan's rotation reveals an internal ocean and changing zonal winds, *Science*, *319*, 1649–1651.

Lorenz, R. D., et al. (2013), A global topographic map of Titan, *Icarus*, *225*, 367–377.

Melosh, H. J. (1977), Global tectonics of a despun planet, *Icarus*, *31*, 221–243.

Melosh, H. J. (2011), *Planetary Surface Processess*, Cambridge Planet. Sci., New York.

Mitri, G., M. T. Bland, A. P. Showman, J. Radebaugh, B. Stiles, R. M. C. Lopes, J. I. Lunine, and R. T. Pappalardo (2010), Moutains on Titan: Modeling and observations, *J. Geophys. Res.*, *115*, E10002, doi:10.1029/2010JE003592.

Nahm, A. L., and R. A. Schultz (2010), Evaluation of the orogenic belt hypothesis for the formation of the Thaumasia Highlands, Mars, *J. Geophys. Res.*, *115*, E04008, doi:10.1029/2009JE003327.

Neish, C. D., and R. D Lorenz (2012), Titan's global crater population: A new assessment, *Planet. Space Sci.*, *60*, 26–33.

Nimmo, F., and B. G. Bills (2010), Shell thickness variations and the long-wavelength topography of Titan, *Icarus*, *208*, 896–904.

Paganelli, F., et al. (2007), Titan's surface from Cassini RADAR SAR and high resolution radiometry data of the first five flybys, *Icarus*, *191*, 211–222.

Pappalardo, R. T., et al. (1998a), Grooved terrain on Ganymede: First results from Galileo high resolution imaging, *Icarus*, *135*, 276–302.

Pappalardo, R. T., J. W. Head, N. D. Sherman, R. Greeley, R. J. Sullivan, and the Galileo Imaging Team (1998b), Classification of Europan ridges and troughs and a possible genetic sequence, 29th Lunar and Planetary Science Conference, Houston, Tex., 2013 March.

Patthoff, D. A., and S. A. Kattenhorn (2011), A fracture history on Enceladus provides evidence for a global ocean, *Geophys. Res. Lett.*, *38*, L18201, doi:10.1029/2011GL048387.

Pechmann, J. B., and H. J. Melosh (1979), Global fracture patterns of a despun planet: Application to Mercury, *Icarus*, *38*, 243–250.

Porco, C. C., et al. (2006), Cassini observes the active south pole of Enceladus, *Science*, *311*, 43–64.

Radebaugh, J., R. D. Lorenz, R. Kirk, J. Lunine, E. R. Stofan, R. M. C. Lopes, S. D. Wall, and the Cassini Radar Team (2007), Mountains on Titan observed by Cassini Radar, *Icarus*, *192*, 77–91.

Radebaugh, J., et al. (2011), Regional geomorphology and history of Titan's Xanadu province, *Icarus*, *211*, 672–685.

Sleep, N. H. (1994), Martian plate tectonics, *J. Geophys. Res.*, *99*, 5639–5655.

Smith-Konter, B., and R. T. Pappalardo (2008), Tidally driven stress accumulation and shear failure of Enceladus's tiger stripes, *Icarus*, *198*, 435–451.

Soderblom, J. M., et al. (2010), Geology of the Selk crater region on Titan from Cassini VIMS observations, *Icarus*, *208*, 905–912.

Solomonidou, A., G. Bampasidis, M. Hirtzig, A. Coustenis, K. Kyriakopoulos, K. St. Seymour, E. Bratsolis, and X. Moussas (2013), Morphotectonic features on Titan and their possible origin, *Planet. Space Sci.*, *77*, 104–117.

Spencer, J. R., et al. (2006), Cassini encounters Enceladus: Background and the discovery of a south polar hot spot, *Science*, *311*, 1401–1405.

Spitale, J., and C. Porco (2007), Association of the jets of Enceladus with the warmest regions on its south-polar fractures, *Science*, *449*, 695–697.

Squyres, S. W. (1982), The evolution of tectonic features on Ganymede, *Icarus*, *52*, 545–559.

Stiles, B. W., S. Hensley, Y. Gim, D. M. Bates, R. L. Kirk, A. Hayes, J. Radebaugh, R. D. Lorenz, K. L. Mitchell, P. S. Callahan, H. Zeblcer, W. T. K. Johnson, C. Veeramacheneni, and the Cassini RADAR Team (2009), Determining Titan surface topography from Cassini SAR data, *Icarus*, *202*, 584–598.

Vening-Meinesz, F. A. (1947), Shear patterns of the Earth's crust, *Trans. AGU*, *28*, 1–61.

Watters, T. R., S. C. Solomon, S. M. Robinson, J. W. Head, S. L. Andre, S. A. Hauck, and S. L. Murchie (2009), The tectonics of Mercury, *Earth Planet. Sci. Lett.*, *285*, 283–296.

Watters, T. R., M. S. Robinson, M. E. Bank, T. Tran, and B. Denevi (2012), Recent extensional tectonics on the Moon revealed by the Lunar Reconnaissance Orbiter Camera, *Nat. Geosci.*, *5*, 181–185.